PHILOSOPHICAL MAGAZINE, 2003, VOL. 83, NO. 9, 1143–1161

Electron-optical phase shift of magnetic nanoparticles II. Polyhedral particles

M. BELEGGIA†§, Y. ZHU†, S. TANDON‡ and M. DE GRAEF‡

† Materials Science Department, Brookhaven National Laboratory, Upton, New York 11973, USA
‡ Department of Materials Science and Engineering, Carnegie Mellon University, Pittsburgh, Pennsylvania 15213, USA

[*Received 25 September 2002 and accepted 9 November 2002*]

ABSTRACT

A method is presented to compute the electron-optical phase shift for a magnetized polyhedral nanoparticle, with either a uniform magnetization or a closure domain (vortex state). The method relies on an analytical expression for the shape amplitude, combined with a reciprocal-space description of the magnetic vector potential. The model is used to construct two building blocks from which more complex structures can be generated. Phase computations are also presented for the five Platonic and 13 Archimedean solids. Fresnel and Foucault imaging mode simulations are presented for a range of particle shapes and microscope imaging conditions.

§ 1. INTRODUCTION

The continuously decreasing length scale of magnetic recording media and other applications based on magnetic nanoparticles necessitates the use of advanced characterization methods, both for chemical and structural analysis and for the study of magnetic domains and magnetic interactions. In recent years, transmission electron microscopes have become equipped with increasingly more sensitive detectors and cameras, and this in turn has improved dramatically the spatial resolution for measurement of chemical compositions, often on the unit-cell length scale. Determination of the fine scale magnetic structure in these materials is essential for the prediction of various material properties. In addition, since virtually all engineering parameters of these materials are directly affected by microstructural features, the nature of these materials makes it necessary to combine closely the study of magnetic structure and microstructure. Lorentz microscopy, and in particular the Fresnel and Foucault observation modes (De Graef 2001), has for several decades been the dominant observation technique for qualitative magnetic domain observations, and this paper deals with the application of Lorentz methods to the study of nanocrystalline magnetic materials.

The study of magnetic domain configurations by means of electron scattering has a long history. The early days of Lorentz microscopy have been summarized by Grundy and Tebble (1968). The basic idea behind the Lorentz observation modes

§ Author for correspondence. Email: beleggia@bnl.gov.

Philosophical Magazine ISSN 1478–6435 print/ISSN 1478–6443 online © 2003 Taylor & Francis Ltd
http://www.tandf.co.uk/journals
DOI: 10.1080/0141861031000066175

is that an electron travelling through a specimen with a non-zero magnetic induction experiences a force, the Lorentz force, normal to both its velocity vector and the local magnetic induction direction. This force causes a net deflection of the electron trajectory away from the path that the electron would follow in the absence of a magnetic induction. The magnitude of the Lorentz deflection angle is usually in the range of a few tens of microradians, or about two orders of magnitude smaller than typical Bragg angles for electron scattering. While the classical formulation provides an intuitive understanding of the scattering of electrons by magnetic foils, for a quantitative analysis one needs to resort to a quantum-mechanical description of the scattering process in terms of the exit wavefunction of the electron.

The increasing importance of nanoscale magnetic particles obviates the need for high-spatial-resolution quantitative observation methods which are capable of elucidating not only the structure and chemistry of the nanoparticles, but also their magnetization state. A quantum-mechanical description of the scattering process requires knowledge of the magnetic phase shift imparted on the beam electron by the particle and its surrounding fringing field. While such a phase shift is relatively easy to compute for a particle with a high symmetry (e.g. a sphere or circular disc), the situation is more complex for a faceted polyhedral nanoparticle. In the present paper, we introduce a theoretical formalism for determining the magnetic component of the electron-optical phase shift for a polyhedral nanoparticle. The method is based on a reciprocal space description of the magnetic vector potential in terms of the shape of the particle, described in detail in the companion paper, part I (Beleggia and Zhu 2003). We apply the method to two classes of polyhedral particles: plate-like particles with a regular polygonal or star shape, and the Platonic and Archimedean solids.

§ 2. General theory

2.1. *Lorentz image formation theory*

Lorentz image contrast simulations require knowledge of two functions: the electron exit wavefunction $\psi(\mathbf{r}_\perp)$ and the transfer function $\mathcal{T}_\mathrm{L}(\mathbf{q}_\perp)$ of the main imaging lens. The exit wavefunction depends on the location $\mathbf{r}_\perp$ in the exit plane and consists of an amplitude and a phase:

$$\psi(\mathbf{r}_\perp) = a(\mathbf{r}_\perp)\exp[\mathrm{i}\varphi(\mathbf{r}_\perp)]. \tag{1}$$

The amplitude varies from one location to the next owing to thickness and local excitation error variations. The phase shift φ consists of two contributions, namely the electrostatic lattice potential $V(\mathbf{r}_\perp, z)$ and the magnetic vector potential $\mathbf{A}(\mathbf{r}_\perp, z)$, and has been described by equation (8) in part I. The electrostatic phase shift depends on the microscope accelerating voltage, whereas the magnetic phase shift is independent of the electron energy.

The microscope transfer function appropriate for Lorentz observation modes is given by

$$\mathcal{T}_\mathrm{L}(\mathbf{q}_\perp) = A(\mathbf{q}_\perp - \mathbf{q}_{\perp 0})\exp(z_2 q^2)\exp(z_4 q^4), \tag{2}$$

with

$$z_2 = -(\pi\theta_c\,\Delta f)^2 + i\pi\lambda\{\Delta f + C_a\cos[2(\phi-\phi_a)]\}, \tag{3a}$$

$$z_4 = -\frac{(\pi\lambda\Delta f)^2}{2} + 2(\pi\theta_c\lambda)^2\,\Delta f\,C_s - i\,\frac{\pi}{2}\,C_s\lambda^3. \tag{3b}$$

In these equations we have the following variables: θ_c, beam divergence angle; Δf, objective lens defocus; C_a, and ϕ_a, magnitude and angle respectively of twofold astigmatism; ϕ, polar angle in the back focal plane; C_s spherical aberration coefficient; $\mathbf{q}_\perp$, spatial frequency conjugate to the exit plane vector $\mathbf{r}_\perp$, where the magnitude of $\mathbf{q}_\perp$ is represented by q. The function $A(\mathbf{q}_\perp - \mathbf{q}_{\perp 0})$ is the aperture function and is unity inside the aperture and zero outside. The vector $\mathbf{q}_{\perp 0}$ defines the centre of the aperture, so that Foucault images can also be considered. For most Lorentz observations, a small-angle approximation can be used, so that the spherical aberration phase shift (imaginary term in z_4) does not contribute significantly to the overall phase shift. From the aberrated wavefunction in the back focal plane, the image intensity can be derived by an inverse Fourier transform

$$I(\mathbf{r}_\perp) = |\mathcal{F}^{-1}[\psi(\mathbf{q}_\perp)]|^2 = |\psi(\mathbf{r}_\perp)\otimes\mathcal{T}_L(\mathbf{r}_\perp)|^2, \tag{4}$$

where $\otimes$ indicates the convolution product and the function $\mathcal{T}_L(\mathbf{r}_\perp)$, the inverse Fourier transform of $\mathcal{T}_L(\mathbf{q}_\perp)$, is the *point spread function* for Lorentz microscopy.

While the computation of the electrostatic phase shift $\varphi_e(\mathbf{r}_\perp)$ is relatively easy if the mean inner potential and the particle shape are known, the magnetic phase shift presents a more difficult challenge. In part I it was shown that, if the magnetization state $\mathbf{m}(\mathbf{r})$ of the particle is known, then the vector potential can be calculated analytically in Fourier space (equation (5) in part I). The magnetic phase shift is then given by equation (10) in part I, which we repeat here for convenience:

$$\varphi_m(k_x,k_y) = \frac{i\pi B_0}{\phi_0}\,\frac{D(k_x,k_y,0)}{k_x^2+k_y^2}\,(\hat{\mathbf{m}}\times\mathbf{k})|_z. \tag{5}$$

The function $D(\mathbf{k})$ is the particle *shape amplitude*, which we shall analyse in more detail in the following section.

2.2. *Particle shape amplitudes*

In the remainder of this paper, we shall consider the case of a polyhedral particle. There are two major reasons for studying polyhedral particles. Firstly, the current interest in the properties of nanoparticles includes not only particles which have solidified or were otherwise formed into a polyhedral shape, but also intentionally shaped particles, such as patterned arrays of discs, plates and so on. A clear understanding of the magnetic behaviour of such particles requires a study of the effect of shape on the magnetization state on the nanoscale and, perhaps more importantly, an analysis of the type of information that can be extracted from electron-optical observations on such particles. An experimental example of magnetic structure imaging in circular, square, triangular and pentagonal cobalt and $Ni_{80}Fe_{20}$ films has been given by Kirk *et al.* (1968). Secondly, the polyhedral shape can be analysed analytically, using a formalism developed by Komrska (1987). Explicit expressions for the shape amplitude can be used to obtain an analytical expression for the electron-optical phase shift. This in turn allows a detailed study of the types of image that can be obtained from either Lorentz microscopy or electron holography. In this section, we shall first describe briefly the shape amplitude formalism. Then we

introduce the types of polyhedral particle for which the phase computations will be carried out.

The shape amplitude $D(\mathbf{k})$ of a polyhedral particle with E edges and F faces is given by (Komrska 1987) (using $\mathbf{k} = 2\pi\mathbf{q}$):

$$D(\mathbf{k}) = -\frac{1}{k^2}\sum_{f=1}^{F}\frac{\mathbf{k}\cdot\mathbf{n}_f}{k^2-(\mathbf{k}\cdot\mathbf{n}_f)^2}\sum_{e=1}^{E_f}L_{fe}\mathbf{k}\cdot\mathbf{n}_{fe}\,\mathrm{sinc}\left(\frac{L_{fe}}{2}\,\mathbf{k}\cdot\mathbf{t}_{fe}\right)\exp(-\mathrm{i}\mathbf{k}\cdot\boldsymbol{\xi}^{\mathrm{C}}_{fe}). \qquad (6)$$

This equation is only valid if the second denominator is non-zero. If $\mathbf{k} = \pm k\mathbf{n}_f$ (in other words, if $\mathbf{k}$ is parallel to any one of the face normals), then the contribution of that particular face (or faces) must be replaced by

$$D_f(\mathbf{k}) = \mathrm{i}\,\frac{\mathbf{k}\cdot\mathbf{n}_f}{k^2}\,P_f\exp(-\mathrm{i}d_f\mathbf{k}\cdot\mathbf{n}_f), \qquad (7)$$

where P_f is the surface area of face f, and d_f is the distance between the origin and face f. In the origin of Fourier space, the shape amplitude is equal to the particle volume, that is $D(\mathbf{0}) = V$. The symbols in equation (6) are defined as follows (figure 1): $\boldsymbol{\xi}^{\mathrm{C}}_{fe}$ are the coordinate vectors of the centre of edge e of face f; $\mathbf{n}_f$ is the unit outward normal to face f; L_{fe} is the length of the eth edge of the fth face; $\mathbf{t}_{fe}$ is the unit vector along the eth edge of the fth face, defined by

$$\mathbf{t}_{fe} = \frac{\mathbf{n}_f\times\mathbf{N}_{fe}}{|\mathbf{n}_f\times\mathbf{N}_{fe}|},$$

where $\mathbf{N}_{fe}$ is the unit outward normal *on* the face which has edge e in common with face f; $\mathbf{n}_{fe}$ is the unit outward normal *in* face f on edge e defined by $\mathbf{n}_{fe} = \mathbf{t}_{fe}\times\mathbf{n}_f$. The input parameters needed to complete this computation for an arbitrary polyhedron are the N_{v} vertex coordinates $\boldsymbol{\xi}_{\mathrm{v}}$ and a list of which vertices make up each face (counterclockwise when looking towards the polyhedron centre). All other quantities can be computed from these parameters.

The shape amplitude formalism can be used to compute the electron-optical phase shift for an arbitrary polyhedral object with a uniform magnetization. It is easy to show that the formalism cannot be applied to particles with a spatially varying magnetization pattern. The derivation of equation (6) relies on the so-called

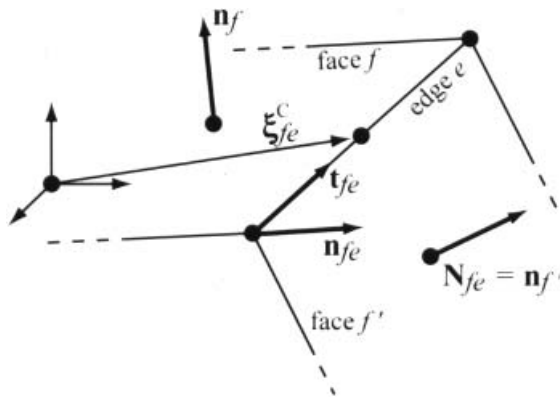

Figure 1. Schematic representation of the face normals $\mathbf{n}_f$, edge vectors $\mathbf{t}_{fe}$ and outward edge normals $\mathbf{n}_{fe}$ used in equation (6).

Abbe transform (Komrska 1987), an integral transform which converts the volume integral of a function Ψ to a surface integral of the outward gradient of Ψ. This transform is valid for all functions Ψ which satisfy the homogeneous Helmholtz equation

$$\Delta\Psi + k^2\Psi = 0. \tag{8}$$

Equation (6) was derived for $\Psi(\mathbf{r}) = \exp(-\mathrm{i}\mathbf{k}\cdot\mathbf{r})$, since this is the integrand of the shape amplitude $D(\mathbf{k})$:

$$D(\mathbf{k}) = \int D(\mathbf{r})\, \exp(-\mathrm{i}\mathbf{k}\cdot\mathbf{r})\, \mathrm{d}\mathbf{r} = \int_V \exp(-\mathrm{i}\mathbf{k}\cdot\mathbf{r})\, \mathrm{d}\mathbf{r}. \tag{9}$$

For a particle with non-uniform magnetization $\mathbf{m}(\mathbf{r})$, the function $\Psi(\mathbf{r})$ would be equal to $\mathbf{m}(\mathbf{r})\exp(-\mathrm{i}\mathbf{k}\cdot\mathbf{r})$. Substitution in the Helmholtz equation results in the component equations

$$\Delta m_i - 2\mathrm{i}\mathbf{k}\cdot\nabla m_i = 0, \tag{10}$$

which can only be satisfied for all $\mathbf{k}$ if $\nabla m_i = \mathbf{0}$, or $\mathbf{m}$ is constant over the volume of the particle. This would appear to restrict the use of equation (6) to uniformly magnetized particles only. However, if a polyhedral particle has multiple magnetic domains, and the magnetization in each domain is uniform, then we can still apply the same formalism by considering each domain as a separate particle and employing the linearity of the shape function.

As shown schematically in figures 2 (*a*) and (*b*), every regular polygonal plate can be viewed as a superposition of isosceles triangular plates, rotated around the central point. If the shape function of the isosceles triangle is represented by $D(\mathbf{r})$, then the pentagonal plate can be described by a sum of five such shape functions, each rotated by 72° around the vertical direction. More generally, any rotation and translation of the building blocks can be taken into account easily by multiplying the shape amplitude by suitable phase terms. Complex particle shapes can hence be constructed from just a few simple building blocks. In each building block, the magnetization can have a different direction. Putting the building blocks together results in domain walls of zero width at the contact planes of the blocks. The introduction of realistic domain walls would only result in a smoothing of the sharp features of the resulting electron-optical phase function, and will not be considered here (for an example of such smoothing, see § 3.1 in part I).

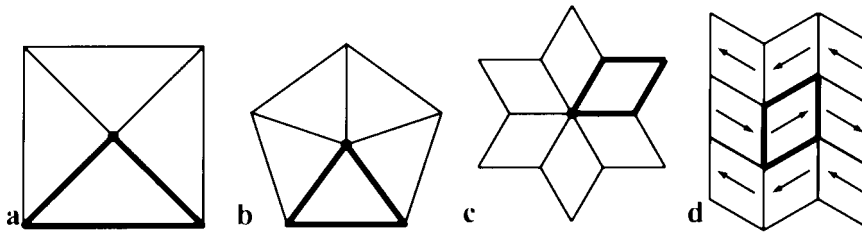

Figure 2. Regular polygonal plates ((*a*) square; (*b*) pentagon) can be constructed by rotating an isosceles triangular plate (outlined) around the central axis. A sheared rectangular plate can be used to create many different shapes, such as (*c*) the hexagonal star and (*d*) a domain structure of intersecting magnetic domain walls often encountered in hard magnetic materials.

In § 3.1 we shall compute the shape amplitude of the isosceles triangular plate. This expression is then generalized to regular polygonal plates in § 3.3. Similarly, star-shaped plates and many planar magnetic domain configurations can be considered to be built from a basic building block, the sheared rectangular plate. In § 3.2 we shall discuss the shape amplitude for a single sheared rectangular plate, and in § 3.3 for a combination of such plates. In § 3.4 we describe the phase computations for the five Platonic and 13 Archimedean polyhedra. Finally, § 3.5 describes a straightforward method to compute the electron-optical phase shift for an arbitrary combination of both building blocks.

§ 3. Applications

3.1. *Isosceles triangular plate*

Consider an isosceles triangular plate with bottom edge length $2a$ and thickness $2c$. The top angle is equal to 2α. The coordinate origin is taken at the centre of the top edge (between vertices 1 and 4), with the coordinate axes as shown in figure 3. The volume of this plate is $V = 2a^2c/\tan\alpha$. The explicit expression for the shape amplitude, derived from equation (6), is given by

$$D(\mathbf{k}) = 4\mathrm{i}c\,\frac{\operatorname{sinc}(ck_z)}{k_x^2 + k_y^2}\sum_{j=1}^{3}\kappa_j \operatorname{sinc}(\mu_j)\exp(\mathrm{i}\nu_j), \tag{11}$$

where $\operatorname{sinc} x \equiv (\sin x)/x$,

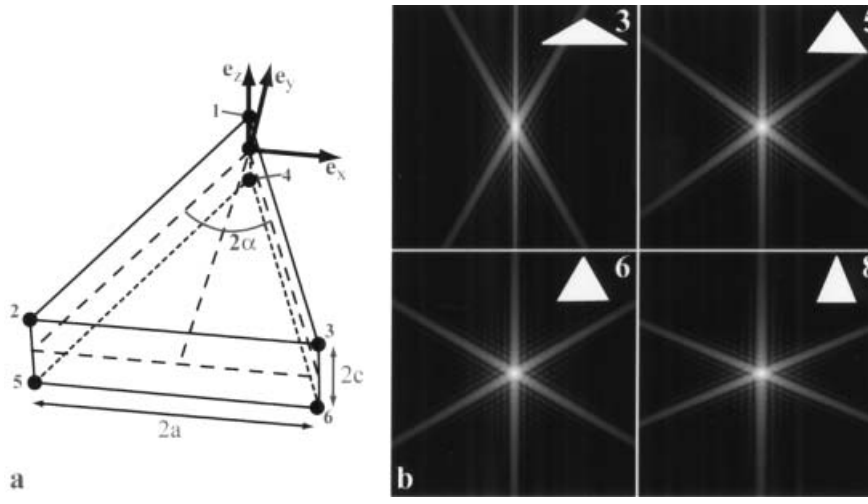

Figure 3. (*a*) Schematic representation of an isosceles triangular plate of thickness $2c$, bottom edge length $2a$ and top angle 2α; (*b*) the shape 'intensity' $|D(k_x, k_y, 0)|^2$ for $2\alpha = 120°$, 72°, 60° and 45°. The isosceles triangular building block is shown in the upper right-hand corner, together with the order of the resulting polygon, that is 5 indicates pentagon, 8 indicates octagon, etc. The intensity scale is logarithmic, to enhance small intensity variations.

$$\kappa_j = \frac{a}{2}\,[-\omega k_x + k_y, \omega k_x + k_y, -2k_y], \tag{12a}$$

$$\mu_j = \frac{a}{2}\,[k_x + \omega k_y, -k_x + \omega k_y, 2k_x], \tag{12b}$$

$$\nu_j = [\mu_1, \mu_2, hk_y] \tag{12c}$$

and $\omega = 1/\tan\alpha$. Along the line $(0, 0, k_z)$ this expression should be replaced by

$$D(0, 0, k_z) = V\,\mathrm{sinc}\,(ck_z). \tag{13}$$

The 'shape intensities', defined by $|D(k_x, k_y, 0)|^2$, for isosceles triangular plates with opening angle $\alpha = 120°, 72°, 60°$ and $45°$ are shown in figure 3 (*b*). As expected, the main intensity 'streaks' are normal to each of the polyhedron faces.

3.2. *Sheared rectangular plate*

The shape amplitude of a sheared rectangular plate with edge lengths $2a$, $2b$ and $2c$ and a shear angle α can be derived from that of a regular rectangular plate of the same dimensions by means of a simple coordinate change. For a rectangular plate we have

$$D(\mathbf{k}) = V\,\mathrm{sinc}\,(ak_x)\,\mathrm{sinc}\,(bk_y)\,\mathrm{sinc}\,(ck_z), \tag{14}$$

with $V = 8abc$; for the sheared plate we obtain

$$D(\mathbf{k}) = V\sin\alpha\,\mathrm{sinc}\,(ak_x)\,\mathrm{sinc}\,\{b[\cos(\alpha k_x) + \sin(\alpha k_y)]\}\,\mathrm{sinc}\,(ck_z). \tag{15}$$

For the origin choice shown in figure 4 (*a*), the shape amplitude must be multiplied by a phase factor:

$$D(\mathbf{k}) \rightarrow D(\mathbf{k})\exp\{-\mathrm{i}[(a + b\cos\alpha)k_x + b\sin(\alpha k_y)]\}. \tag{16}$$

The shape intensities for two different shearing angles α are shown in figure 4 (*b*).

3.3. *Regular polygonal plates*

Any regular polygonal plate can be constructed by rotating an isosceles triangular plate of the proper dimensions around the $\mathbf{e}_z$ axis. If we denote the number of triangles needed by N_t, then the top angle 2α must be equal to $2\pi/N_t$. The resulting shape function is given by

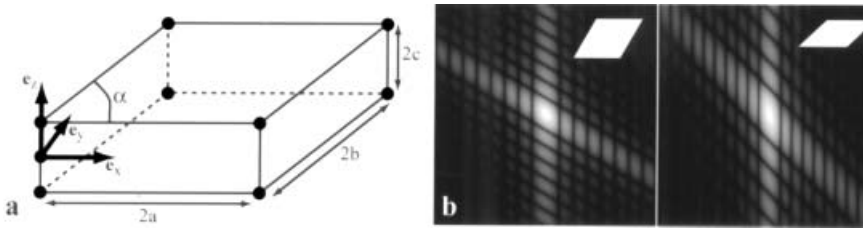

Figure 4. (*a*) Schematic representation of a sheared rectangular plate of dimensions $2a$, $2b$ and $2c$, and shear angle α; (*b*) the shape 'intensity' $|D(k_x, k_y, 0)|^2$ for dimensions $(2a, 2a, 2c)$ with $\alpha = 60°$ and for dimensions $(4a, 2a, 2c)$, with $\alpha = 45°$ (logarithmic intensity scale).

$$D(\mathbf{k}) = 4\mathrm{i}c\,\frac{\operatorname{sinc}(ck_z)}{k_x^2 + k_y^2}\sum_{p=1}^{N_\mathrm{t}}\sum_{j=1}^{3}\kappa_{pj}\operatorname{sinc}(\mu_{pj})\exp(\mathrm{i}\nu_{pj}) \tag{17}$$

$$= \sum_{p=1}^{N_\mathrm{t}} D_p(\mathbf{k}),$$

with

$$\kappa_{pj} = [c_p\kappa_1 + s_p\mu_1, c_p\kappa_2 - s_p\mu_2, -a(s_pk_x + c_pk_y)], \tag{18a}$$

$$\mu_{pj} = [c_p\mu_1 - s_p\kappa_1, c_p\mu_2 + s_p\kappa_2, a(c_pk_x - s_pk_y)], \tag{18b}$$

$$\nu_{pj} = [\mu_{p1}, \mu_{p2}, h(s_pk_x + c_pk_y)] \tag{18c}$$

and $c_p = \cos(\theta_0 + \theta_p)$, $s_p = \sin(\theta_0 + \theta_p)$; θ_0 is an overall rotation angle fixing the orientation of the bottom edge of the first triangular plate with respect to the $\mathbf{e}_x$ axis, and $\theta_p = 2p\alpha$. Positive rotation angles represent counterclockwise rotations.

Figure 5 shows the shape 'intensities' $|D(k_x, k_y, 0)|^2$ for $N_\mathrm{t} = 3, 4, 5, 6, 7$ and 8. For odd N_t, the shape amplitude is complex and the lack of inversion centre combined with Friedel's law results in an apparent symmetry axis of order $2N_\mathrm{t}$. For $N_\mathrm{t} = 4$ we find the familiar result $D(k_x, k_y, 0) = 8a^2c\operatorname{sinc}(ak_x)\operatorname{sinc}(ak_y)$. Star-shaped polygonal plates can be constructed in a similar way, starting from equation (15) for the sheared rectangular plate.

3.4. *Platonic and Archimedean solids*

The electron-optical phase shift for an arbitrary polyhedral solid can be computed by direct application of equation (10) in part I. The five Platonic and 13 Archimedean shapes are listed in table 1. For each polyhedron, the number of

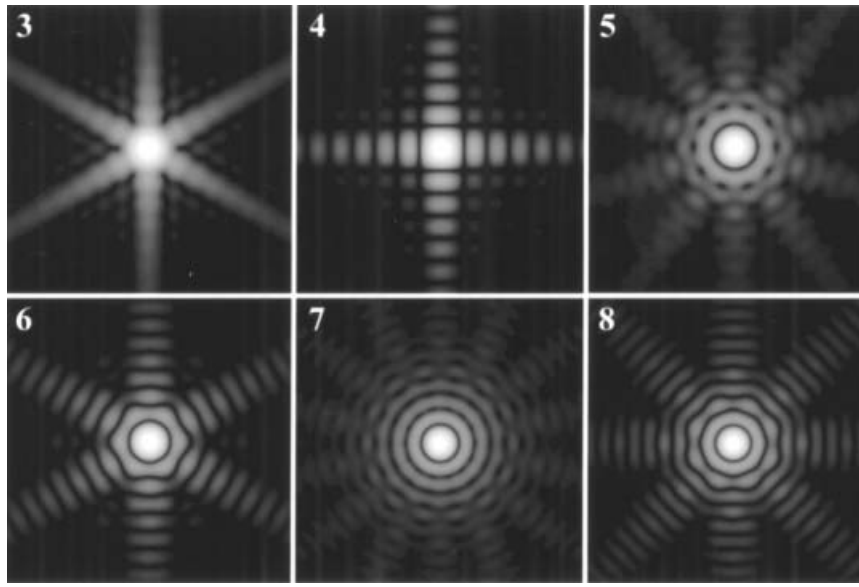

Figure 5. Shape 'intensities' for the regular polygonal plates of order $N_\mathrm{t} = 3$, 4, 5, 6, 7 and 8. All functions were computed using equation (17).

Table 1. Numbers N_v of vertices, numbers N_e of edges and numbers N_f of faces for the five Platonic and 13 Archimedean solids, together with the volume factors V_s. The total volume is given by $V = V_s L^3$, with L the edge length. The edge length L for a volume of 10^6 nm^3 is shown in the sixth column.

Polyhedron	N_v	N_e	N_f	V_s	L (nm)	Figure
Tetrahedron	4	6	4	0.118	204.0	6 (*a*)
Cube	8	12	6	1.000	100.0	6 (*b*)
Octahedron	6	12	8	0.471	128.5	6 (*c*)
Dodecahedron	20	30	12	7.663	50.72	6 (*d*)
Icosahedron	12	30	12	2.182	77.10	6 (*e*)
Truncated octahedron	24	36	14	11.31	44.54	6 (*f*)
Cuboctahedron	12	24	14	2.357	75.14	6 (*g*)
Rhombitruncated cuboctahedron	48	72	26	41.80	28.81	6 (*h*)
Snub cube	24	60	38	7.890	50.23	6 (*i*)
Rhombicuboctahedron	24	48	26	8.714	48.59	6 (*j*)
Truncated cube	24	36	14	13.60	41.89	6 (*k*)
Truncated icosahedron	60	90	32	55.29	26.25	6 (*l*)
Icosidodecahedron	30	60	32	13.84	41.65	6 (*m*)
Rhombitruncated icosidodecahedron	120	180	62	206.8	16.91	6 (*n*)
Snub dodecahedron	60	150	92	37.62	29.84	6 (*o*)
Rhombicosidodecahedron	60	120	62	41.61	28.86	6 (*p*)
Truncated dodecahedron	60	90	32	85.04	22.74	6 (*q*)
Truncated tetrahedron	12	18	8	2.711	71.72	6 (*r*)

vertices, edges and faces is shown, as well as the volume factor V_s. To compute the actual volume, V_s must be multiplied by L^3, where L is the edge length. V_s was computed numerically for each polygon by taking the limit of $D(\mathbf{k})$ for $\mathbf{k} \rightarrow \mathbf{0}$ with $L_{fe} = 1$. The sixth column of table 1 shows the edge length L in nanometres for a particle volume $V = 10^6$ nm^3. In § 4, the magnetic and electrostatic phase shift will be computed for all Platonic and Archimedian polyhedral shapes. They will be compared with the magnetic phase shift for a uniformly magnetized spherical particle of the same volume. It can be shown (De Graef *et al.* 1999) that the phase shift for a spherical particle of radius R and saturation induction B_0 along the $\mathbf{e}_x$ direction is described in real space by†

$$\varphi_m(\mathbf{r}_\perp) = \frac{2}{3}\frac{\pi}{\phi_0} B_\perp \frac{y}{r^2}\{R^3 - [R^2 - (r^2 < R^2)]^{3/2}\}, \tag{19}$$

with $r^2 = x^2 + y^2$ and the symbol $(a < b)$ indicates that the smaller of a and b should be used. The Fourier transform of this expression is given by equation (19) in part I:

$$\varphi_m(k_x, k_y) = \frac{4\pi^2 \mathrm{i}}{\phi_0} B_\perp R^2 \frac{k_y}{k_\perp^3} j_1(k_\perp R), \tag{20}$$

with $k_\perp^2 = k_x^2 + k_y^2$ and $j_1(x) = (\mathrm{sinc}\, x - \cos x)/x$ the spherical Bessel function of first order.

† A factor of $\frac{2}{3}$ was inadvertently omitted from equation (2) in the paper by De Graef *et al.* (1999).

3.5. *Electron-optical phase shift computation*

The phase shift due to the magnetic vector potential of a regular polygonal plate can be computed analytically by application of equation (10) in part I. If the beam direction is represented by means of the two spherical angles ϕ and θ, then it is easy to show that the Fourier transform of the phase shift in a plane normal to the beam direction is given by

$$\varphi_{\mathrm{m}}(k'_x, k'_y) = \frac{\mathrm{i}\pi B_0}{\phi_0} \sum_{p=1}^{N_{\mathrm{t}}} \frac{D_p(k'_x, k'_y, K)}{k'^2_x + k'^2_y + K^2}\, \mathcal{S}(\mathbf{k}', \theta_0, \theta_p, \theta, \phi), \tag{21}$$

where D_p was defined in equation (17),

$$K = -(k'_x \cos\phi + k'_y \sin\phi) \tan\theta, \tag{22}$$

and the components (k'_x, k'_y) are given by

$$k'_x = k_x \cos\phi \cos\theta - k_y \sin\phi, \tag{23a}$$

$$k'_y = k_x \sin\phi \cos\theta + k_y \cos\phi. \tag{23b}$$

The two-dimensional inverse Fourier transform of equation (21) results in the electron-optical phase shift $\varphi_{\mathrm{m}}(x', y')$, where (x', y') are coordinates in the plane normal to the electron beam. The y' coordinate is measured along the projection of $\mathbf{e}_z$ into the image plane. The components k_x and k_y are the frequency components with respect to the object reference frame. They are symmetrically sampled around the reciprocal space origin.

The function $\mathcal{S}$ in equation (21) depends on the magnetization state of the polygonal plate. For a uniformly magnetized plate, with magnetization direction $\hat{\mathbf{m}} = m_\perp(\cos\theta_m\, \mathbf{e}_x + \sin\theta_m\, \mathbf{e}_y) + m_z \mathbf{e}_z$, we have

$$\begin{aligned} \mathcal{S} = {} & (m_z \sin\phi \sin\theta - m_\perp \sin\theta_m \cos\theta) k'_x \\ & + (m_\perp \cos\theta \cos\theta_m - m_z \cos\phi \sin\theta) k'_y \\ & + m_\perp \sin\theta \sin(\theta_m - \phi)\, K. \end{aligned} \tag{24}$$

For the vortex state, with the magnetization parallel to the bottom edge of each isosceles triangular plate, we have

$$\begin{aligned} \mathcal{S} = {} & \cos\theta\, [k'_y \sin(\theta_m + \theta_p) + k'_x \cos(\theta_m + \theta_p)] \\ & - K \sin\theta \sin(\theta_m + \theta_p + \phi). \end{aligned} \tag{25}$$

These equations are valid provided that $\theta \neq \pi/2$. The Fourier transform of the phase is undefined in the origin, and it is convenient to select $\varphi_{\mathrm{m}}(\mathbf{k} = \mathbf{0}) = 0$, resulting in a real-space phase function with zero average.

Finally, for computations in which multiple particles are present in the same field of view, it is convenient to apply the coordinate translation by means of a phase factor in reciprocal space. A polygonal plate with centre at $\mathbf{R}_{\mathrm{s}}$ can be obtained by multiplication of the shape amplitude with a phase factor

$$D_p(\mathbf{k}) \rightarrow D_p(\mathbf{k}) \exp(-\mathrm{i}\mathbf{R}_{\mathrm{s}} \cdot \mathbf{k}). \tag{26}$$

The electrostatic phase shift $\varphi_{\mathrm{e}}(\mathbf{r}_\perp)$ can be computed directly from the shape amplitude by performing an integration along the electron trajectory. If the electro-

static potential is constant over the volume of the particle, then the electrostatic phase shift can be expressed as

$$\varphi_e(\mathbf{r}_\perp) = \sigma V_0 \int_{-\infty}^{+\infty} D(\mathbf{r}_\perp, \ell)\, \mathrm{d}\ell = \sigma V_0 t_p, \tag{27}$$

with t_p the projected thickness. This integral can be computed for an arbitrary incident beam orientation using the same formalism as used to derive equation (21). The resulting phase is then proportional to the projected thickness of the particle. If we assume that the particle does not diffract electrons, that is, only the mean inner potential is of importance, then the projected thickness can also be used to compute the amplitude of the electron exit wave using a straightforward exponential absorption law. The total exit wave is then described by

$$\psi(\mathbf{r}_\perp) = \exp[-\mu t_p(\mathbf{r}_\perp)] \exp\{\mathrm{i}[\varphi_m(\mathbf{r}_\perp) + \varphi_e(\mathbf{r}_\perp)]\}, \tag{28}$$

where the absorption factor μ can be taken as the inverse of the normal absorption length ξ_0' (De Graef 2003). If the nanoparticle is supported by an amorphous film, typically a carbon film, then this would add an additional phase factor to the exit wavefunction (Fan and Cowley 1987).

§4. Examples of phase computations

4.1. *Phase maps for selected particle shapes*

Figure 6 shows the magnetic and electrostatic phase shifts for all Platonic and Archimedean shapes. For each polyhedron, a pair of grey-scale images is shown. The image on the left corresponds to the difference between the magnetic phase shift for the uniformly magnetized polyhedron and the magnetic phase shift for the uniformly magnetized sphere with the same volume (radius, 62.03 nm). The volume was taken to be $10^6\,\mathrm{nm}^3$ for all particles, so that the edge length corresponds to the values shown in table 1. All magnetic phase shift differences are shown on a common intensity scale with minimum -0.630 rad (black) and maximum 0.630 rad (white). The extremal phase shifts for the uniformly magnetized sphere are ± 3.941 rad. This implies that the face shift for a polyhedral particle may locally be up to about 15% different from that for a sphere of the same volume. In the fringing field area, the phase shifts for all particles are identical with that for the sphere. This is because at a large distance the fringing field for all particles approaches that of a magnetic dipole. The phase difference images in figure 6 indicate that, in order to determine the magnetic component of the phase shift, both a high spatial resolution and a high phase resolution are required. Furthermore, the electrostatic phase shift, discussed next, will be added to the magnetic phase shift, complicating the determination of the magnetization state of the particle.

The electrostatic phase shift is proportional to the projected thickness, which is shown as a grey-scale plot on the right-hand side of each pair of images in figure 6. Superimposed on the projected thickness is a projection of the polyhedron in the orientation used for the computation. The fine structure of both magnetic and electrostatic phases depends sensitively on the precise orientation of the polyhedron. Figure 7 shows the phase shift along a line normal to the magnetization direction and through the centre of the polyhedron for the five Platonic shapes and the equal volume sphere. The vertical line indicates the radius of the sphere. As expected, the cube shows a discontinuous phase behaviour because it is oriented such that the

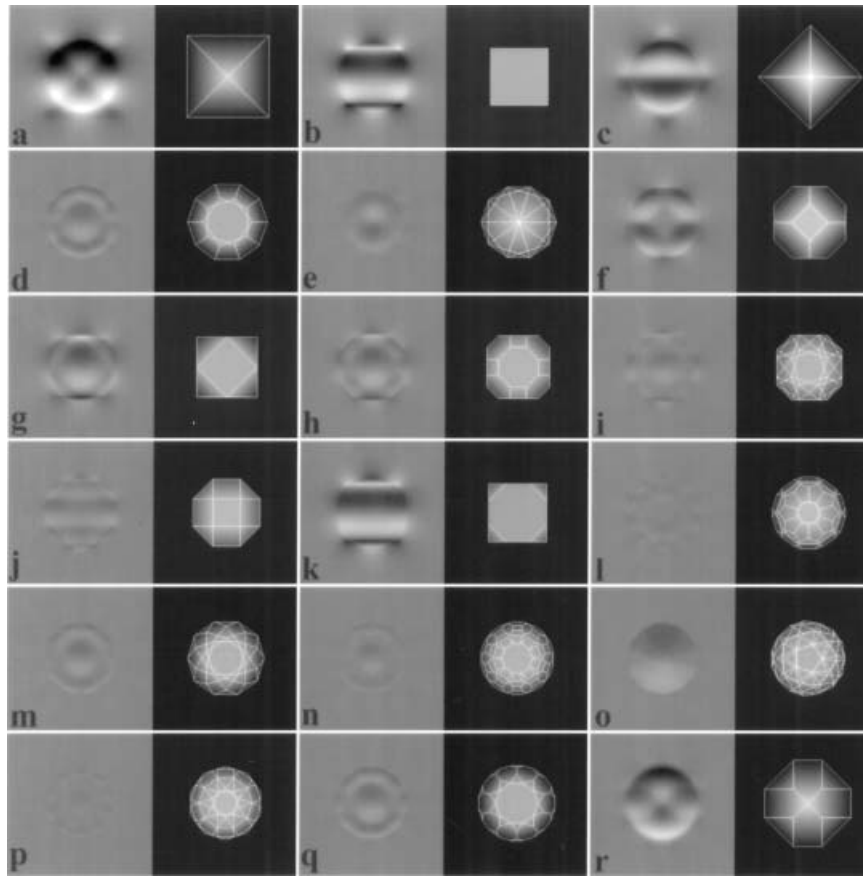

Figure 6. Magnetic and electrostatic phase shifts for the 5 Platonic and 13 Archimedean shapes. All particles have identical volumes ($10^6\,\mathrm{nm}^3$). The magnetic phase shifts are divided by the phase shift for an equal volume sphere with the same magnetization. The contrast variations represent the ratio range $[-0.630, 0.630]$. The projected edge drawing of each polyhedron is superimposed on the electrostatic phase shift. (*a*)–(*r*) refer to the entries in the last column of table 1.

incident beam is parallel to the side faces. The phase shift for the icosahedron is nearly identical with that of the equal volume sphere. This is again to be expected, since the icosahedral shape is nearly spherical. The differences between the various phase curves show that faceting of nanoparticles can have a subtle effect on the magnitude of the magnetic phase shift. A high phase resolution will be required to measure these phase differences.

As an illustration of the magnetic and electrostatic phase computations for the disc-shaped particles based on the isosceles-triangular and the sheared-rectangular building block, we shall consider an array of eight particles, as shown in figure 8 (*a*). Four of the particles are constructed using the isosceles triangle, and the other four using the sheared rectangle. The magnetization states are indicated by means of vectors representing the direction of $\mathbf{M}_0$. The four particles on the left have a thickness of 20 nm, and the others are 10 nm thick. The saturation induction is $B_0 = 1\,\mathrm{T}$ for all particles. The computational array measures 512×512 pixels, and the scale factor is 2 nm per pixel, resulting in an viewing area of about $1\,\mu\mathrm{m}^2$.

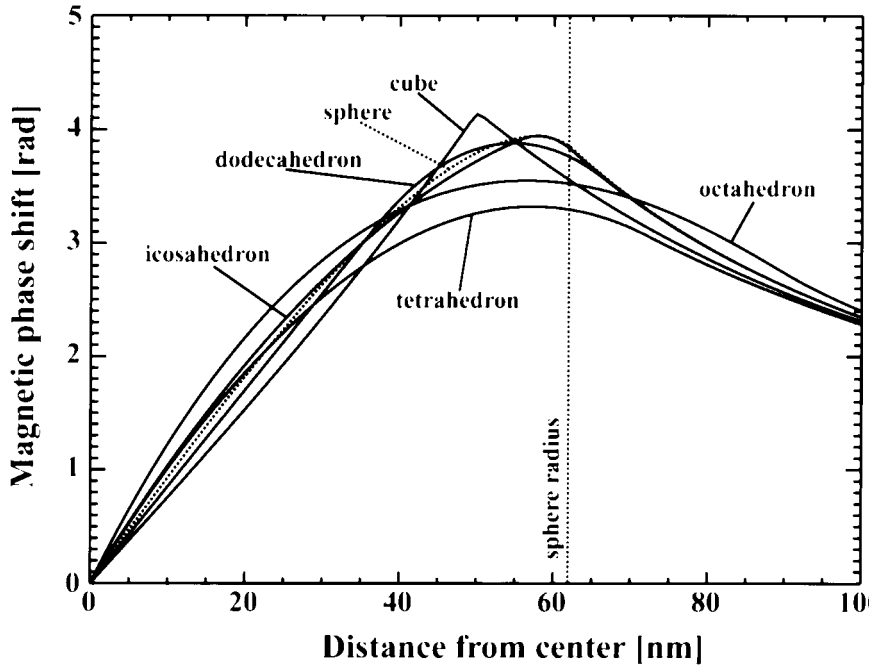

Figure 7. Magnetic phase shift along a line normal to the magnetization direction and through the centre of the polyhedron for the 5 Platonic shapes and the equal volume sphere. All particles have a volume of $10^6\,\mathrm{nm}^3$ and identical saturation magnetic induction of 1 T.

Figure 8 (*b*) shows the magnetic phase shift φ_m, together with $\cos(5\varphi_m)$ (figure 8 (*c*)). The triangular and pentagonal discs have vortex magnetization states with opposite polarities, and the resulting phase profiles are pyramidal shapes with positive or negative slopes. There is no fringing field around these particles. All uniformly magnetized particles (first and third rows) are surrounded by a dipole field; the formalism correctly includes the interactions between these particles through the linearity of the vector potential and resulting phase shift. The two particles in the right-most column have a vortex magnetization state, but there is a weak fringing field around the sharp points of the star shape. The magnetic phase shift ranges from −8.097 to 5.194 rad.

The electrostatic phase shift is shown in figure 8 (*d*); the phase shift vanishes in between the particles and is proportional to the projected thickness t_p wherever a particle is present. The electrostatic phase shift ranges from 0 to 11.01 rad. The total phase shift $\varphi_m + \varphi_e$ and the cosine of five times the total phase shift are shown in figure 8 (*e*) and (*f*) respectively. The total phase shift ranges from −3.725 to 15.91 rad. The particle arrangement shown in figure 8 (*a*) will be used in the following sections to illustrate Fresnel and Foucault image formation.

4.2. *Fresnel and Foucault image computations*

Figure 9 shows a combination of simulated Fresnel and Foucault images for the particle arrangement in figure 8 (*a*). The centre image is the in-focus image for the following imaging parameters: accelerating voltage, 200 kV; beam divergence

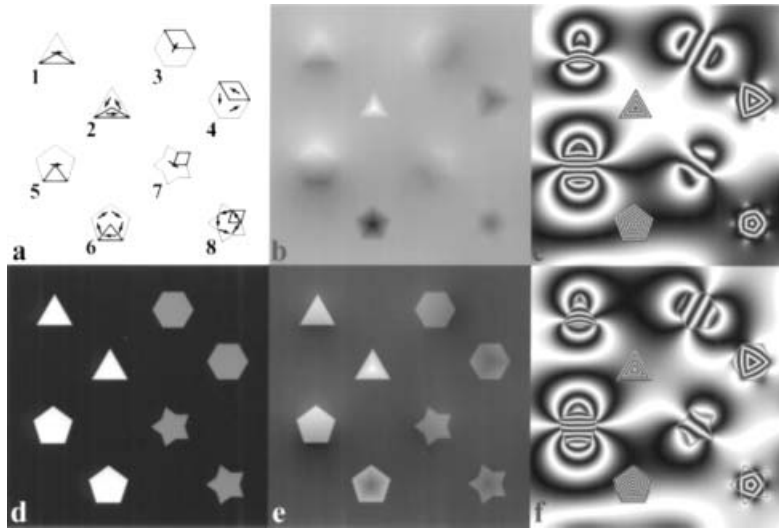

Figure 8. (*a*) Configuration of 8 disc-shaped particles, based on the isosceles-triangular and the sheared-rectangular building blocks, where magnetization states are indicated by the direction of the vector, and the building block of each particle is outlined; (*b*) magnetic phase shift φ_m; (*c*) $\cos(5\varphi_m)$; (*d*) φ_e for an accelerating voltage of 200 kV; (*e*) $\varphi_e + \varphi_m$; (*f*) $\cos[5(\varphi_e + \varphi_m)]$.

angle $\theta_c = 10^{-6}$ rad; aperture radius, $2\,\mathrm{nm}^{-1}$; spherical aberration $C_s = 1$ m; defocus spread, 10 μm. The normal absorption length is taken to be $\xi_0' = 50$ nm. The saturation induction of the particles is taken to be $B_0 = 1$ T, and the mean inner potential is $V_0 = 20$ V. The particles are 'supported' by an amorphous film 20 nm thick with a mean inner potential of 10 V.

The top left and right images show simulated under-focus and over-focus images at a defocus value $\Delta f = \pm 0.5$ mm. The electrostatic component of the over-focus image is shown in the lower left image. This image was computed by putting $B_0 = 0$ T and leaving all other parameters unchanged. The magnetic component of the same image is shown on the lower right, with $V_0 = 0$ V. It is clear that the magnetic component of the image is rather subtle and gives rise to either an asymmetry in the Fresnel fringes, or an off-centre shift of the contrast inside the particle. This is particularly clear for particles 3 and 7, using the numbering scheme of figure 8 (*a*). The bright dot in the centre of particle 6 is caused by the magnetic phase shift and is typical for particles with a vortex magnetization state. The magnetic contribution to the Fresnel images decreases with decreasing particle size. It is hence difficult to prove unambiguously that a magnetic component of the image contrast is present. Furthermore, since the magnetic phase shift causes an asymmetry of the Fresnel fringes surrounding the particle, the standard method of correcting image astigmatism by ensuring that the Fresnel fringe is symmetric all around the particle must not be used if a magnetic phase shift contribution is expected. With the exception of the central bright or dark dot in flat particles with a vortex state, there is, in general, no contrast inversion as a function of defocus. This is quite different from the image characteristics of magnetic domain walls in foils of constant thickness, where the contrast reversal is used to identify the location of the domain wall.

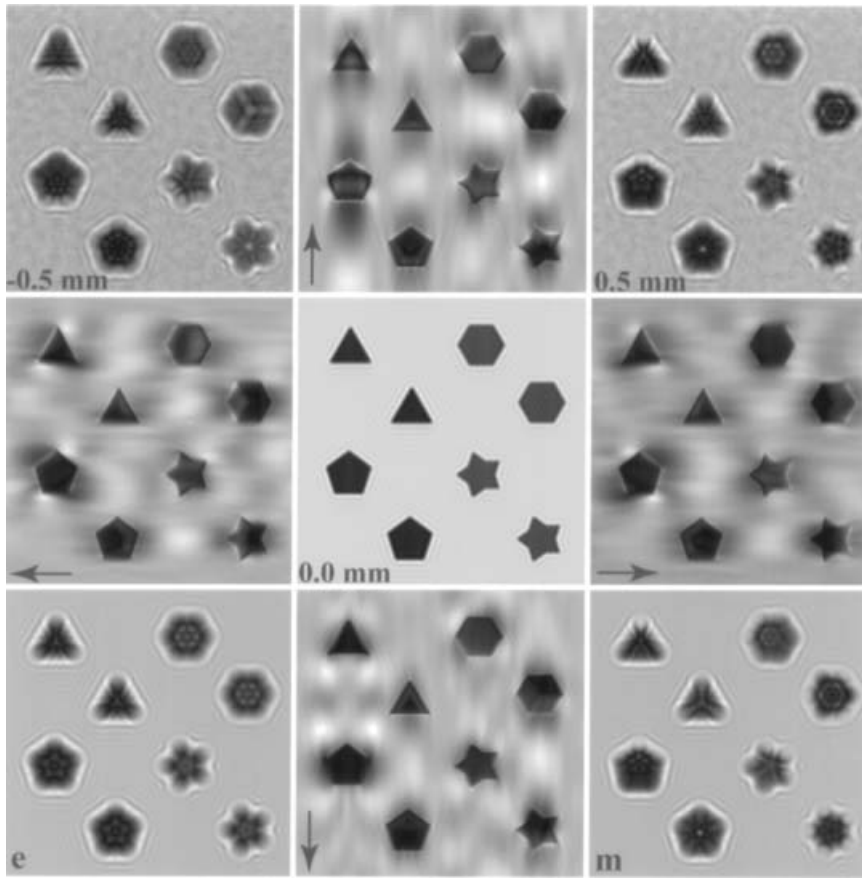

Figure 9. Montage of Fresnel and Foucault images for the particle configuration of figure 8 (*a*). The in-focus image is shown in the centre, under-focus and over-focus images are shown at the top left and top right respectively. The bottom left and bottom right images represent the electrostatic and magnetic components respectively, of the over-focus image (top right). Foucault images are indicated by the arrows in the lower left corner of each image. The imaging parameters are as follows: 200 kV; $\theta_c = 10^{-6}$ rad; aperture radius, $2\,\mathrm{nm}^{-1}$; aperture shift, $1.9\,\mathrm{nm}^{-1}$.

The remaining four images in figure 9 are Foucault images, obtained by shifting the centre of the diffraction aperture by a vector $\mathbf{q}_0$. The magnitude of the aperture shift is equal to 0.95 times the aperture radius, and the direction of the shift is indicated by the arrows in the lower left corner of each image. Dark and bright contrast lobes can be observed around the particles with uniform magnetization states, while magnetic domains are clearly present in the particles with vortex states. The Foucault contrast sensitively depends on the precise position of the aperture edge with respect to the optical axis. Figure 10 shows a sequence of Foucault images for particle 2 (triangular with vortex state), for horizontal and vertical aperture shifts. The magnitude of the shift is indicated as a fraction of the aperture radius. The central image has the aperture edge precisely on the optical axis. The image contrast varies significantly when the aperture is moved only a small distance. While it is straightforward to compute Foucault-type images, it is not easy to position the

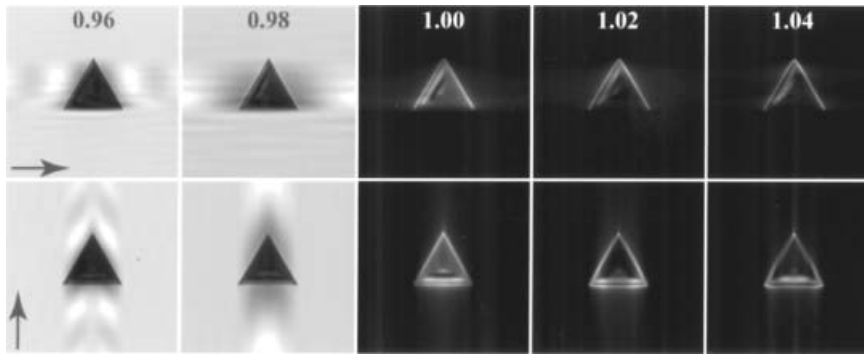

Figure 10. Foucault images for horizontal (top row) and vertical (bottom row) aperture shifts. The aperture shifts are indicated in units of the aperture radius. The object is a triangular plate of thickness 20 nm, and the viewing area measures 500 nm × 500 nm. The triangle has a vortex magnetization state.

aperture reproducibly in an experiment. It is crucial, however, that the aperture be perfectly centred for the observation of magnetic nanoparticles in the Fresnel imaging mode, since small aperture shifts can cause contrast features that are similar to those caused by residual astigmatism.

Figure 11 shows Fresnel image contrast for four different polyhedra: 1, octahedron; 2, icosahedron; 3, truncated cube; 4, snub dodecahedron. The top row shows a through-focus series for the following imaging parameters: 200 kV; $\theta_c = 10^{-5}$ rad; aperture radius, 2 nm^{-1}. The defocus is measured in millimetres, and the field of view is 500 nm × 500 nm. The top row of figure 11 shows the Fresnel images for $V_0 = 20$ V and $B_0 = 1$ T; the magnetization vector points from left to right. The bottom row has identical imaging conditions, except that there is no magnetic contribution ($B_0 = 0$ T). The only signature of the magnetic phase shift is a slight vertical asymmetry of the Fresnel fringes. For the icosahedron and snub dodecahedron, which more closely approximate a sphere, the circular Fresnel fringes are shifted off-centre

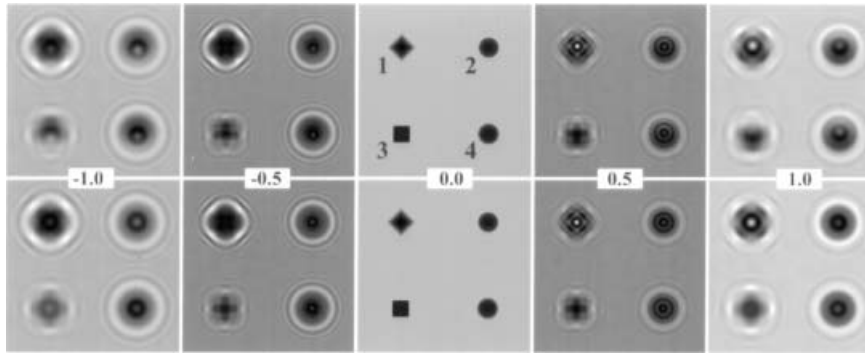

Figure 11. Fresnel through-focus series for four polyhedral shapes (1, octahedron; 2, icosahedron; 3, truncated cube; 4, snub dodecahedron). The microscope imaging parameters are as follows: 200 kV; $\theta_c = 10^{-5}$ rad; aperture radius, 2 nm^{-1}; $V_0 = 20$ V; $B_0 = 1$ T. For the bottom row, the phase shift is entirely electrostatic, that is $B_0 = 0$. The viewing area has dimensions of 500 nm × 500 nm.

by the magnetic phase shift, consistent with the phase shift model for a uniformly magnetized sphere (De Graef *et al*. 1999). Note that a fairly large defocus value is needed to bring out the contrast asymmetries. This leads to a significant magnification of the particle; the apparent particle size in the defocused images is about three to four times larger than the actual particle size.

4.3. *Magnetic induction maps*

With the recent advances in phase reconstructions from experimental data, either through the use of electron holography (Völkl and Lehmann 1999) or via the transport-of-intensity equation (Paganin Nugent 1998), it has become 'fashionable' to display so-called *magnetic induction maps*. These maps are typically derived from the phase by means of the following equation (Chapman 1989):

$$\nabla\varphi = -\frac{\pi}{\phi_0}\,(\mathbf{B}\times\mathbf{n})t, \tag{29}$$

where $\mathbf{B}$ is the magnetic induction, $\mathbf{n}$ a unit vector parallel to the incident electron beam and t the foil thickness. The magnetic induction components derived from this equation are (for a right-handed Cartesian reference frame with $\mathbf{n} = -\mathbf{e}_z$)

$$(B_x, B_y) = \frac{\phi_0}{\pi t}\left(-\frac{\partial\varphi}{\partial y}, \frac{\partial\varphi}{\partial x}\right). \tag{30}$$

It is important to point out the conditions under which this equation may be used. The reconstructed phase φ is usually the total phase, which consists of both an electrostatic contribution φ_e and a magnetic contribution φ_m. The gradient operation would give meaningless results on the electrostatic component of the phase, which in turn means that φ_e must be constant. This is only possible if the foil thickness t is constant over the region of interest. Furthermore, since the electron-optical phase shift represents the integral of the vector potential along the electron trajectory, the phase only has a simple relation to the magnetic induction components inside the particle if there is no fringing field. This means that equation (29) may only be used if there are no fringing fields above or below the particle or foil.

Consider the following numerical example: a magnetic ring is constructed by taking 40 isosceles triangles with top angle $\pi/20$, height h and magnetization $\mathbf{m}$, and subtracting from the resulting plate a slightly smaller plate, constructed from triangular plates of height $h - 2c$ and magnetization $-\mathbf{m}$. This ring has a square cross-section. Next, we compute the gradient of the phase for two different magnetization configurations: vortex state and uniformly magnetized. Figure 12 (*a*) shows the resulting phase, figure 12 (*b*) shows the cosine of the phase, and figures 12 (*c*) and (*d*) show the magnetic induction components B_x and B_y respectively. White represents an induction component along the positive $\mathbf{e}_x$ and $\mathbf{e}_y$ directions. The computed magnetic induction map for the vortex state agrees well with the input state. Equation (29) is applicable in this case since there is no fringing field. For the uniformly magnetized state, with $\hat{\mathbf{m}} = \mathbf{e}_x$, the phase (figure 12 (*e*)) is not constant outside the ring. This is due to the fringing field which is taken into account in all simulations in this paper. The gradient operation on this phase function results in the magnetic induction maps in figures 12 (*g*) and (*h*). For B_x the agreement with the input phase is good only near the top and bottom of the ring, whereas the B_y component should vanish completely. As a rule of thumb we can state that equation

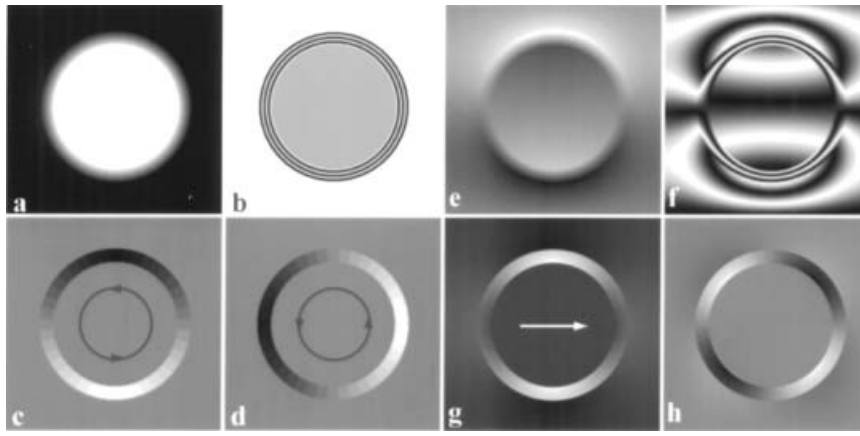

Figure 12. Phase simulation and magnetic induction components (following equation (29)) for a double ring consisting of 40 isosceles triangles, where the centre ring has the opposite magnetization pattern, resulting in zero magnetization inside the ring: (*a*)–(*d*) the counterclockwise vortex state; (*e*)–(*h*) the uniformly magnetized state.

(29) should only be applied to a reconstructed phase if there is no phase variation outside the particle.

§ 5. Conclusions

In this paper and its companion paper (part I) we have shown that it is possible to compute the magnetic and electrostatic phase shift components for a wide range of particle shapes. The main feature of this model relies on a Fourier space description of the magnetic vector potential $\mathbf{A}$. While part I dealt with rectangular, cylindrical and spherical shapes with various magnetization states, part II provides an analysis of the computation of the magnetic and electrostatic phase shifts for polyhedral particles.

Through the use of isosceles triangular plates and sheared rectangular plates, for which analytical expressions for the shape amplitude $D(\mathbf{K})$ are provided, more complex three-dimensional shapes can be built with either a uniform or a vortex magnetization state. Once the phase shift is known in analytical or numerical form, the standard image formation framework for high-resolution electron microscopy can be used to compute images for the Fresnel and Foucault imaging modes. Examples of simulations showing characteristic magnetic image features are shown for several particle shapes. The phase computation algorithm introduced in parts I and II opens the way to quantitative phase reconstruction and interpretation for magnetic nanoparticles of arbitrary shape. Experimental research on polyhedral magnetic ferrite nanoparticles is currently under way.

Acknowledgement

The authors would like to acknowledge the US Department of Energy, Basic Energy Sciences, for financial support under contracts DE-FG02-01ER45893 and DE-AC02-98CH10886.

References

Belleggia, M., and Zhu, Y., 2003, *Phil. Mag.*, **83**, 1043.
Chapman, J., 1989, *Mater. Sci. Engng*, **B3**, 355.
De Graef, M., 2001, *Magnetic Microscopy and its Applications to Magnetic Materials*, edited by M. De Graef and Y. Zhu (New York: Academic Press), chapter 2, pp. 27–67.
De Graef, M., 2003, *Introduction to Conventional Transmission Electron Microscopy* (Cambridge University Press).
De Graef, M., Nuhfer, N., and McCartney, M., 1999, *J. Microsc.*, **194**, 84.
Fan, G., and Cowley, J., 1987, *Ultramicroscopy*, **21**, 125.
Grundy, P., and Tebble, R., 1968, *Adv. Phys.*, **17**, 153.
Kirk, K. J., McVitie, S., Chapman, J. N., and Wilkinson, C. D. W., 2001, *J. appl. Phys.*, **89**, 7174.
Komrska, J., 1987, *Optik*, **80**, 171.
Paganin, D., and Nugent, K., 1998, *Phys. Rev. Lett.*, **80**, 2586.
Völkl, E., and Lehmann, M., 1999, *Introduction to Electron Holography*, edited by E. Völkl, L. Allard and D. Joy (New York: Kluwer), chapter 6, pp. 125–151.